

# Spin waves and three-dimensionality in the high-pressure antiferromagnetic phase of $\text{SrCu}_2(\text{BO}_3)_2$

Ellen Fogh,<sup>1</sup> Gaétan Girit,<sup>1</sup> Mohamed E. Zayed,<sup>2</sup> Andrea Piovano,<sup>3</sup> Martin Boehm,<sup>3</sup>  
 Paul Steffens,<sup>3</sup> Irina Saffulina,<sup>3</sup> Ursula B. Hansen,<sup>3</sup> Stefan Klotz,<sup>4</sup> Jian-Rui Soh,<sup>1</sup>  
 Ekaterina Pomjakushina,<sup>5</sup> Frédéric Mila,<sup>6</sup> Bruce Normand,<sup>1,7</sup> and Henrik M. Rønnow<sup>1</sup>

<sup>1</sup>*Laboratory for Quantum Magnetism, Institute of Physics,  
 Ecole Polytechnique Fédérale de Lausanne (EPFL), CH-1015 Lausanne, Switzerland*

<sup>2</sup>*Department of Physics, Carnegie Mellon University in Qatar, Education City, PO Box 24866, Doha, Qatar*

<sup>3</sup>*Institut Laue-Langevin (ILL), 71 avenue des Martyrs, 38042 Grenoble, France*

<sup>4</sup>*Sorbonne Université, UMR CNRS 7590, Institut de Minéralogie,  
 de Physique des Matériaux et de Cosmochimie (IMPMC), Paris, France*

<sup>5</sup>*Laboratory for Multiscale Materials Experiments,  
 Paul Scherrer Institute, CH-5232 Villigen PSI, Switzerland*

<sup>6</sup>*Institute of Physics, Ecole Polytechnique Fédérale de Lausanne (EPFL), CH-1015 Lausanne, Switzerland*

<sup>7</sup>*Laboratory for Theoretical and Computational Physics,  
 Paul Scherrer Institute, CH-5232 Villigen-PSI, Switzerland*

Quantum magnetic materials can provide explicit realizations of paradigm models in quantum many-body physics. In this context,  $\text{SrCu}_2(\text{BO}_3)_2$  is a faithful realization of the Shastry-Sutherland model (SSM) for ideally frustrated spin dimers, even displaying several of its quantum magnetic phases as a function of pressure. We perform inelastic neutron scattering (INS) measurements on  $\text{SrCu}_2(\text{BO}_3)_2$  at 5.5 GPa and 4.5 K, observing spin waves that characterize the high-pressure antiferromagnetic phase. The experimental spectra are well described by linear spin-wave calculations on a SSM with an inter-layer interaction, which is determined accurately as  $J_c = 0.053(3)$  meV. The presence of  $J_c$  indicates the need to account for the three-dimensional nature of  $\text{SrCu}_2(\text{BO}_3)_2$  in theoretical models, also at lower pressures. We find that the ratio between in-plane interactions,  $J'/J = 1.8(2)$ , undergoes a dramatic change compared to lower pressures that we deduce is driven by a sharp drop in the dimer coupling,  $J$ . Our results underline the wide horizons opened by high-pressure INS experiments on quantum magnetic materials.

Frustrated magnetic interactions give rise to fascinating entangled quantum states, including valence-bond solids, quantum spin liquids, and spin ices [1]. Beyond the Heisenberg model on frustrated geometries such as the triangular and kagome lattices, exotic ground states, excitations, and quantum phase transitions (QPTs) are found in many systems where interactions compete in real space or in spin space. Despite multiple developments in both theoretical and numerical methods, the nature of many such states, their spectra, and the model phase diagrams remain only partially understood. Experimental studies of materials providing physical realizations are therefore an essential factor for our understanding of quantum magnetic systems.

$\text{SrCu}_2(\text{BO}_3)_2$  is an ideally frustrated system composed of  $\text{Cu}^{2+}$  dimers ( $S = 1/2$  spin pairs) arranged orthogonally both in and between quasi-two-dimensional (2D) layers, as represented in Figs. 1(a)-(c) [2]. The in-plane network realizes the Shastry-Sutherland model (SSM) [inset Fig. 1(d)], proposed [3] for its exact dimer-singlet ground state at small  $J'/J$  and governed by this ratio of competing interactions [4–9].  $\text{SrCu}_2(\text{BO}_3)_2$  exhibits the dimer-singlet ground state at ambient pressure [2, 10–14] and is well described by a SSM with  $J'/J = 0.63$  and additional weak (3%) Dzyaloshinskii-Moriya (DM) interactions [15–19]. Remarkably, the phase diagram of  $\text{SrCu}_2(\text{BO}_3)_2$  under an applied hydrostatic pressure [20–

22], shown in Fig. 1(d), mirrors that of the SSM with increasing  $J'/J$  [Fig. 1(e)], and is studied extensively for its exotic QPTs [23–25]. Above 4 GPa, where the tetragonal symmetry changes to monoclinic [26–28], antiferromagnetic (AFM) order is found by neutron and X-ray diffraction [21, 27, 29] and phase-transition features are reported around 8 K [23] and above 120 K [23, 27, 28]. However, these high pressures pose a severe challenge to experiment and rather little is known about either the precise pressure regimes for the SSM-AFM and monoclinic-AFM phases or the possible magnetic interactions in either phase.

Here we perform an inelastic neutron scattering (INS) experiment to characterize the monoclinic-AFM phase of  $\text{SrCu}_2(\text{BO}_3)_2$ . Working at 5.5 GPa and 4.5 K, we observe dispersive spin-wave excitations in 58 mg of sample. Linear spin-wave theory is appropriate to deduce the parameters of the minimal magnetic Hamiltonian. The in-plane interactions change dramatically from  $J'/J = 0.63$  at ambient pressure to  $1.8(2)$  at 5.5 GPa, which we ascribe to a strong reduction of  $J$  arising from its near-critical bond angle. We also discover that it is necessary to include an inter-layer coupling, which we fit as  $J_c = 0.053(3)$  meV, to explain the observed 2 meV splitting of otherwise degenerate branches in the low-energy part of the spectrum. We discuss the consequences of this 3D nature for the physics of  $\text{SrCu}_2(\text{BO}_3)_2$ .

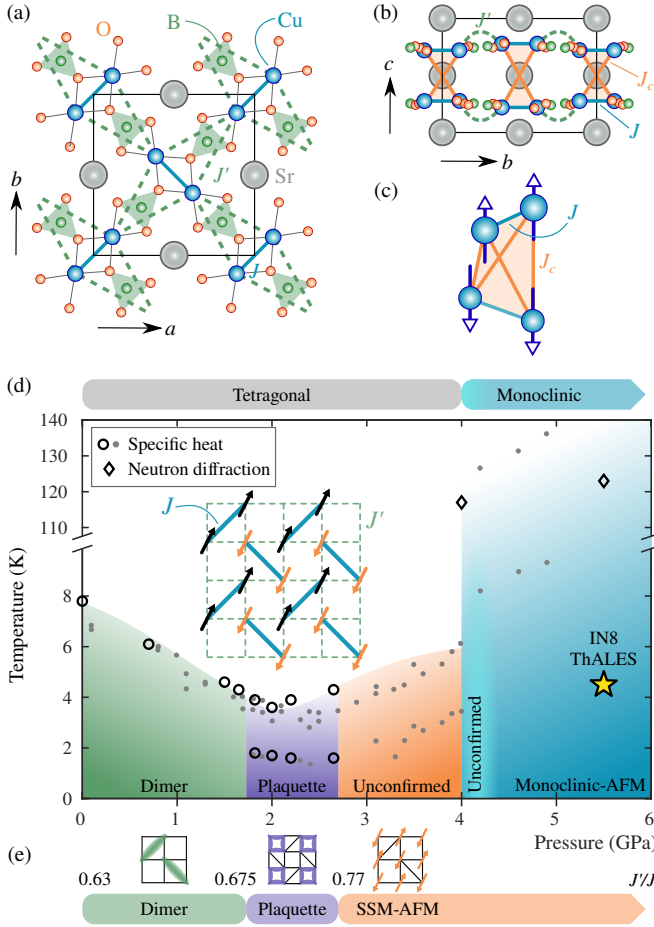


FIG. 1.  $\text{SrCu}_2(\text{BO}_3)_2$  and the Shastry-Sutherland model (SSM). (a)-(b) Crystal structure of  $\text{SrCu}_2(\text{BO}_3)_2$  shown in projection along  $(0, 0, 1)$  (a) and  $(1, 0, 0)$  (b). The dimer interaction,  $J$  (solid blue line), inter-dimer interaction,  $J'$  (dashed green line), and inter-layer interaction,  $J_c$  (solid orange line), are indicated. (c) Illustration of the tetrahedron formed by two orthogonal dimers stacked along the  $(0, 0, 1)$  direction. (d) Phase diagram of  $\text{SrCu}_2(\text{BO}_3)_2$  as a function of temperature and pressure, as deduced from specific-heat measurements (circles [24] and dots [23]) and neutron diffraction (diamonds) [21, 27]. The star marks the location in temperature and pressure of our INS experiments. The inset shows a schematic representation of the SSM. (e) Phase diagram of the SSM as a function of  $J'/J$ , as determined by multiple numerical methods [4–9].

Our INS experiments used a 58 mg disc-shaped single-crystalline sample of  $\text{SrCu}_2(\text{BO}_3)_2$ , whose growth and characterization we summarize in Sec. S1A of the Supplemental Material (SM) [30]. The sample was oriented with  $\mathbf{Q} = (q_h, q_k, 0)$  in the horizontal scattering plane. Its small size is a challenge for INS, but recent developments in high-pressure techniques at the Institute Laue-Langevin (ILL) [40–42] made this experiment possible. Using a Paris-Edinburgh press, the pressure was increased gradually to 5.5 GPa while the lattice parameters of  $\text{SrCu}_2(\text{BO}_3)_2$  [26] were measured for pressure de-

termination. The sample chamber was pre-cooled with liquid  $\text{N}_2$  and cooling to 4.5 K was provided by a closed-cycle refrigerator. We performed two consecutive experiments at the IN8 and ThALES triple-axis spectrometers with the same loading. We used fixed momentum transfers  $k_f = 2.66 \text{ \AA}^{-1}$  at IN8 and  $k_f = 1.50 \text{ \AA}^{-1}$  at ThALES, providing respective instrumental resolutions (FWHM) of 1.05(1) and 0.167(4) meV. Scans with constant energy transfer,  $E$ , or constant momentum transfer,  $\mathbf{Q}$ , were performed with typical counting times of 5 min per point. In the SM [30] we provide detailed descriptions of the pressure loading procedure (Sec. S1B), instrument configurations (Sec. S1C), pressure determination (Sec. S1D), and data treatment (Sec. S1E). Supporting diffraction data were collected at IN3, also at the ILL, and this experiment is described in Sec. S1F.

A selection of constant- $E$  and constant- $\mathbf{Q}$  scans is shown in Fig. 2, with data from both IN8 and ThALES. The width of the elastic line on IN8 allowed for access to energy transfers above approximately 2 meV, whereas at ThALES 0.5 meV was accessible. Because the in-plane lattice parameters of the monoclinic phase satisfy  $a/b \simeq 0.999$  (with monoclinic angle  $\beta \simeq 94^\circ$ ) [27], we retain the tetragonal approximation and use  $a^* = b^* = 2\pi/a$ . The color contours in Figs. 3(a)-(b) collect all neutron intensities measured respectively along  $(0, q_k, 0)$  and  $(q_h, 1, 0)$  at constant  $E$ , and make clear that dispersive modes are present with minima at  $(0, 1, 0)$  and  $(1, 1, 0)$ . At 1.5 meV and below, we no longer observe neutron intensity at  $(0, 1, 0)$  [Figs. 2(b) and 2(c)]. Above 5 meV it becomes difficult to discern sharp modes due to vanishing neutron intensity [Figs. 2(a) and 2(d)]. In Figs. 2(a)-(b) we fitted the data collected along  $(q_h, 1, 0)$  with Gaussian line shapes centered respectively at  $\pm\delta_h$  and  $\pm\delta'_h$  from  $(0, 1, 0)$  and  $(1, 1, 0)$ , allowing the peak widths and intensities to vary individually (Sec. 1E of the SM [30]). Similar fits to the data collected along  $(0, q_k, 0)$  yielded mode positions along both directions in  $\mathbf{Q}$ . The dispersion minimum at  $(0, 1, 0)$  is resolved in a constant- $\mathbf{Q}$  scan from ThALES [Fig. 2(c)]. A Gaussian fit yields an energy of 1.90(8) meV and the magnetic origin of the excitation is demonstrated by its absence at 140 K. In Fig. 2(d), we show constant- $\mathbf{Q}$  scans from IN8 where subtraction of the incoherent contribution allowed the fitting of one or two Gaussian profiles at different  $\mathbf{Q}$ . The fitted mode positions are marked in Figs. 3(a)-(b), where the relatively large error bars in the high-energy range reflect the difficulty in determining the excitation structure here.

From the near-tetragonal nature of the high-pressure phase, we assume that the SSM continues to provide a minimal model for the observed spin-wave dispersion. The physics of the AFM phase is that the stronger  $J'$  forces the spins to order ferromagnetically (FM) on the dimers and AFM between dimers, both in and out of plane [Fig. 1(c)]. The 2D AFM phase has two doubly

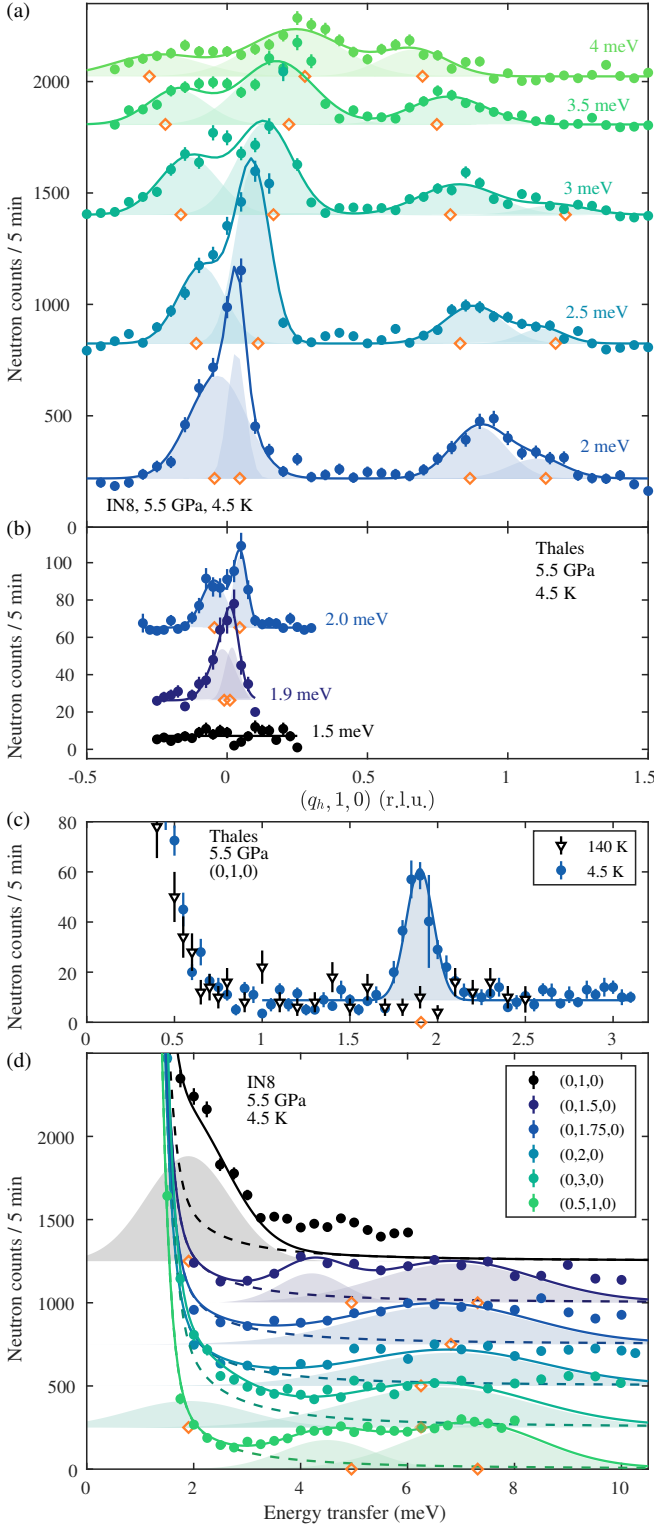


FIG. 2. Selection of INS data collected at IN8 and ThALES at 5.5 GPa. (a)-(b) Constant- $E$  scans along  $\mathbf{Q} = (q_h, 1, 0)$ . (c)-(d) Constant- $\mathbf{Q}$  scans. Fits to determine the mode positions in  $\mathbf{Q}$  and  $E$  are illustrated with solid lines and the shaded areas represent the individual Gaussians. Dashed lines in panel (d) show the incoherent scattering contribution measured across the elastic line at  $(0.7, 1.3, 0)$ . Orange symbols mark the predicted mode centers obtained in a global parameter fit.

degenerate spin-wave branches, a Goldstone mode and an optical mode. Although we have no dispersion measurements in the  $c$  direction, the observed in-plane scattering intensity [Figs. 3(a)-(b)] motivates the introduction of an inter-layer interaction,  $J_c$ , between orthogonal dimers along the  $(0, 0, 1)$  direction, as shown in Fig. 1(c). This model has the following properties: (i) the degeneracy of the low-energy mode is lifted, with a splitting  $\Delta = 8S\sqrt{J'J_c}$  above the massless point; (ii) due to the AFM inter-layer stacking, the intensity of the Goldstone mode vanishes at  $\mathbf{Q} = (0, 1, 0)$  and  $(0, 3, 0)$ , making the spectrum look gapped at these positions; (iii) there is an intensity asymmetry along  $(0, q_k, 0)$  around  $q_k = 1$  and 3, caused by the orthogonal arrangement of the dimers in the plane; (iv) the splitting between the low-energy and optical branches at the top of the former [e.g.  $\mathbf{Q} = (0, 1.5, 0)$  and  $(0.5, 1, 0)$ ] is  $\Delta' \approx 2SJ$ .

We refine the model parameters based on the experimentally determined mode positions and intensities with assistance from SPINW [43], a software implementation of linear spin-wave theory, to obtain  $J' = 4.28(14)$  meV,  $J = 2.36(26)$  meV (i.e.  $J'/J = 1.8(2)$ ), and  $J_c = 0.053(3)$  meV. The predicted mode positions are shown in Fig. 2 as the orange symbols. The model spectra for an assumed instrumental energy resolution of 1 meV are shown in Figs. 3(c)-(d), and provide good agreement with the measurements in Figs. 3(a)-(b). In particular, the fitted spectrum confirms an AFM layer stacking, because FM stacking would result in Goldstone-mode intensity at  $(0, 1, 0)$  and  $(0, 3, 0)$ , but not at  $(1, 1, 0)$ . We note that our deduced parameter values are not corrected for the quantum renormalization factor,  $Z_c$ , which to our knowledge has not been evaluated for the AFM phase of the SSM.

Currently the most refined estimates for the interaction parameters of  $\text{SrCu}_2(\text{BO}_3)_2$  at ambient pressure are  $J = 81.5$  K (7.0 meV) and  $J' = 51.3$  K (4.4 meV,  $J'/J = 0.63$ ) [19]. While there is no exact model for the increase of  $J'/J$  with pressure, a linear decrease of both  $J$  and  $J'$ , with  $\Delta J/P$  falling 3-4 times faster than  $\Delta J'/P$  [21], reproduces the  $(H, P)$  phase diagram rather well in the dimer and plaquette phases [19]. *Ab initio* calculations predict a discontinuity in the parameters on entering the SSM-AFM phase [44], and at higher pressures no information for  $J$  or  $J'$  was available until now. Although it is unexpected that  $J$  is suppressed so strongly, it is not implausible. Its size and sign are highly sensitive to the Cu-O-Cu bond angle following the Goodenough-Kanamori rules [45, 46], especially when this angle is close to  $95^\circ$  [47]. Measurements in  $\text{SrCu}_2(\text{BO}_3)_2$  [Figs. 1(a)-(b)] indicate a decrease from  $98^\circ$  at ambient pressure to  $94^\circ$  at 3.7 GPa [29]. The  $J'$  superexchange path is through a  $\text{BO}_3$  unit, which remains robust with pressure and locked in position by a mirror plane, becoming free to rotate out of the plane only beyond the monoclinic transition. Our results therefore quantify all of these considerations.

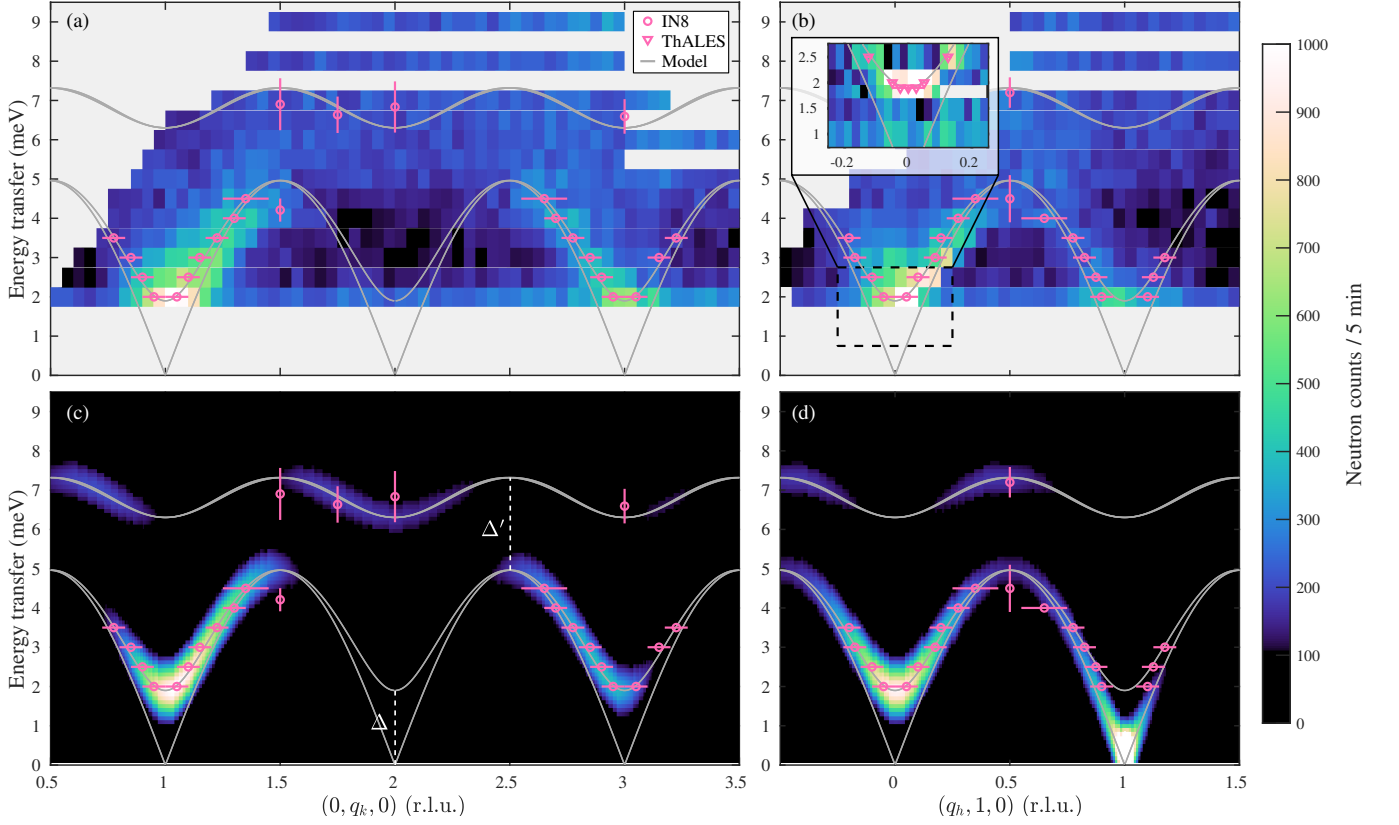


FIG. 3. Measured and modeled excitation spectra of  $\text{SrCu}_2(\text{BO}_3)_2$  in the monoclinic-AFM phase. (a)-(b) INS intensity collected on IN8 at 5.5 GPa and 4.5 K, shown as a function of  $E$  and  $\mathbf{Q}$  along  $(0, q_k, 0)$  and  $(q_h, 1, 0)$ . The inset in panel (b) shows lower-energy data (dashed box) collected at ThALES around  $(0, 1, 0)$ . (c)-(d) Comparison with the spectrum calculated using an energy resolution of 1 meV. The splittings  $\Delta$  and  $\Delta'$  are indicated in panel (c). Mode positions determined from the INS data are shown by pink circles (IN8) and triangles (ThALES); the orientation of the error bar indicates whether a point originates from a constant- $E$  or constant- $\mathbf{Q}$  scan. The grey curves show the dispersion calculated from linear spin-wave theory.

Turning to  $J_c$ , we note first that the system is much softer along the  $\hat{c}$  direction than in the plane, with the  $c$  lattice parameter reduced by around 6% at 5.5 GPa, whereas  $a$  and  $b$  are reduced by less than 1% [26, 27]. The buckling of the  $\text{Cu-BO}_3$  planes shown in Fig. 1(b) leads to two independent  $J_c$  parameters [16]. However, the in-plane INS spectrum is sensitive only to their combined effect, and thus we fit a single effective  $J_c$ ; further details are presented in Sec. S2A of the SM [30]. In this quasi-2D system, the splitting  $\Delta$  is a steep function of  $J_c$  and in our INS experiment  $\Delta = 1.90(8)$  meV is measured to high accuracy, making our estimate of  $J_c = 0.053(3)$  meV at 5.5 GPa very precise. Although this small value reflects the absence of significant inter-layer superexchange paths, it is still thought that  $J_c$  has stronger contributions from superexchange than from direct exchange, making its evolution under pressure difficult to predict. Nevertheless, the ambient-pressure  $J_c$  is unlikely to be much larger than 0.05 meV. An indirect estimate of 0.7 meV, an order of magnitude above our result, was obtained as a 10% correction to the high-temperature magnetic susceptibility [16, 48], but was pre-

sumably a consequence of strong finite-size effects inherent to early numerical studies (since remedied by more modern technology [49]).

Although a Heisenberg SSM with an inter-layer coupling captures all the measured features of the spin-wave dispersion in the high-pressure phase, we draw attention to two key points. First,  $\text{SrCu}_2(\text{BO}_3)_2$  has weak DM interactions at ambient pressure [16, 17, 19]. These terms also act to gap the Goldstone mode, but the DM interaction required to create a gap of 1.9 meV in a 2D SSM is  $0.7J'$ , as we show in Sec. 2B of the SM [30], making this a very unlikely mechanism to explain the INS spectrum. In our minimal model, we absolutely do not claim that DM interactions are no longer present, only that we cannot resolve them. In Sec. 2B we show also that even 10% DM terms in the lower-symmetry monoclinic phase of  $\text{SrCu}_2(\text{BO}_3)_2$  would provide only a minor correction to the Heisenberg interaction parameters. Second, we stress that linear spin-wave theory does not account for two-magnon scattering, possible two-magnon bound states, or any other effects of quantum fluctuations caused by the frustration remaining in the system, all of which, as



we summarize in Sec. 2C of the SM [30], could contribute to the broad and weak neutron intensities observed above 5 meV in Figs. 2(d) and 3(a)-(b).

The confirmation of a small  $J_c$  is essential information for assessing the suitability of a 2D SSM to describe  $\text{SrCu}_2(\text{BO}_3)_2$ . The fact that the dimer ( $J$ ) bonds are forced into a FM configuration in the AFM phase makes the four  $J_c$  bonds in an inter-layer tetrahedron fully unfrustrated [Fig. 1(c)], and hence they contribute an energy of order 1 K per site to the stability of a 3D AFM phase. In the dimer-singlet phase, by contrast, these bonds are simply ineffective. Concerning the plaquette phase, it was shown rather early that its very existence depends on having only a weak  $J_c$  [50], and the propensity of  $J_c$  to destabilize the plaquette phase has been used recently to extract a value  $J_c \approx 0.2$  meV [51]. Our definitive  $J_c$  can be used to refine the estimates of intra-layer energetics and their pressure evolution on which that estimate was based. Another delicate issue is whether the plaquette singlets form around the squares that contain the dimer bond (“full plaquette”) [21] or the squares that do not (“empty plaquette”) [7]. The minimal  $J_c$  we consider should not affect plaquette formation [51], but too little is known about the 3D plaquette order to make a statement on whether more complex inter-layer coupling could do so. Finally, because the plaquette-AFM transition of the 2D SSM has been proposed as a candidate deconfined quantum critical point (DQCP), and  $\text{SrCu}_2(\text{BO}_3)_2$  as a candidate material for its observation [52–54], the effects of inter-layer coupling should definitely be included as part of evaluating such a scenario.

Finally, we remark that our results do not provide an immediate understanding of the reported phase transitions at 8 K [23] and 120 K [23, 27, 28], the parameters of our quasi-2D model being more likely to favor a single ordering transition at an intermediate temperature (of order  $J'/2$  [55]). We performed detailed diffraction studies of the (0, 1, 0) magnetic Bragg peak, as described in Sec. S1F of the SM [30], finding an unconventional thermal evolution with a characteristic temperature of 88 K. While one may speculate about the onset of 2D and of true 3D order, these contradictions underline the need for more systematic combined studies of the structure and magnetism at and above 3 GPa.

In conclusion, we have performed INS on a single crystal of 58 mg to measure spin waves in the monoclinic-AFM phase of  $\text{SrCu}_2(\text{BO}_3)_2$  at a pressure of 5.5 GPa. The observed spectra are well described by a Shastry-Sutherland model with an inter-layer coupling. Consequently, when modelling the physics of the  $\text{SrCu}_2(\text{BO}_3)_2$  phase diagram, it may be necessary to consider the three-dimensionality. Our work highlights the importance of the technical capability to perform INS under extreme conditions of high pressure and low temperature for the discovery and investigation of quantum magnetic states.

*Acknowledgements* – We are very grateful to C. Payre

and J. Maurice for their technical assistance with the high-pressure equipment at the ILL. We acknowledge the financial support of the European Research Council through the Synergy network HERO (Grant No. 810451) and of the Swiss National Science Foundation through Project Grant No. 188648. We thank the ILL for the allocation of neutron beam time for this study on the IN8, ThALES, and IN3 spectrometers. Collected data are available as Refs. [56, 57]. This publication was made possible in part by the generous support of the Qatar Foundation through the Seed Research Funding Program of Carnegie Mellon University in Qatar. The statements made herein are solely the responsibility of the authors.

- 
- [1] L. Savary and L. Balents, “Quantum spin liquids: a review,” *Rep. Prog. Phys.* **80**, 016502 (2016).
  - [2] H. Kageyama, K. Yoshimura, R. Stern, N. V. Mushnikov, K. Onizuka, M. Kato, K. Kosuge, C. P. Slichter, T. Goto, and Y. Ueda, “Exact dimer ground state and quantized magnetization plateaus in the two-dimensional spin system  $\text{SrCu}_2(\text{BO}_3)_2$ ,” *Phys. Rev. Lett.* **82**, 3168 (1999).
  - [3] B. S. Shastry and B. Sutherland, “Exact ground state of a quantum mechanical antiferromagnet,” *Physica B+C* **108**, 1069 (1981).
  - [4] A. Koga and N. Kawakami, “Quantum Phase Transitions in the Shastry-Sutherland Model for  $\text{SrCu}_2(\text{BO}_3)_2$ ,” *Phys. Rev. Lett.* **84**, 4461 (2000).
  - [5] C. H. Chung, J. B. Marston, and S. Sachdev, “Quantum phases of the Shastry-Sutherland antiferromagnet: Application to  $\text{SrCu}_2(\text{BO}_3)_2$ ,” *Phys. Rev. B* **64**, 134407 (2001).
  - [6] A. Läuchli, S. Wessel, and M. Sigrist, “Phase diagram of the quadrumerized Shastry-Sutherland model,” *Phys. Rev. B* **66**, 014401 (2002).
  - [7] P. Corboz and F. Mila, “Tensor network study of the Shastry-Sutherland model in zero magnetic field,” *Phys. Rev. B* **87**, 115144 (2013).
  - [8] H. Nakano and T. Sakai, “Third Boundary of the Shastry-Sutherland Model by Numerical Diagonalization,” *Journal of the Physical Society of Japan* **87**, 123702 (2018).
  - [9] N. Xi, Hongyu Chen, Z. Y. Xie, and R. Yu, “Plaquette valence bond solid to antiferromagnet transition and deconfined quantum critical point of the Shastry-Sutherland model,” *Phys. Rev. B* **107**, L220408 (2023).
  - [10] S. Miyahara and K. Ueda, “Exact dimer ground state of the two-dimensional Heisenberg spin system  $\text{SrCu}_2(\text{BO}_3)_2$ ,” *Phys. Rev. Lett.* **82**, 3701 (1999).
  - [11] H. Kageyama, M. Nishi, N. Aso, K. Onizuka, T. Yoshihama, K. Nukui, K. Kodama, K. Kakurai, and Y. Ueda, “Direct evidence for the localized single-triplet excitations and the dispersive multitriplet excitations in  $\text{SrCu}_2(\text{BO}_3)_2$ ,” *Phys. Rev. Lett.* **84**, 5876 (2000).
  - [12] H. Kageyama, K. Onizuka, Y. Ueda, M. Nohara, H. Suzuki, and H. Takagi, “Low-temperature specific heat study of  $\text{SrCu}_2(\text{BO}_3)_2$  with an exactly solvable ground state,” *J. Exp. Theor. Phys.* **90**, 129 (2000).
  - [13] B. D. Gaulin, S. H. Lee, S. Haravifard, J. P. Castellan, A. J. Berlinsky, H. A. Dabkowska, Y. Qiu, and J. R. D.

- Copley, “High-Resolution Study of Spin Excitations in the Singlet Ground State of  $\text{SrCu}_2(\text{BO}_3)_2$ ,” *Phys. Rev. Lett.* **93**, 267202 (2004).
- [14] K. Kakurai, K. Nukui, N. Aso, M. Nishi, H. Kadowaki, H. Kageyama, Y. Ueda, L.-P. Regnault, and O. Cépas, “Neutron Scattering Investigation on Quantum Spin System  $\text{SrCu}_2(\text{BO}_3)_2$ ,” *Prog. Theor. Phys. Suppl.* **159**, 22 (2005).
- [15] O. Cépas, K. Kakurai, L. P. Regnault, T. Ziman, J. P. Boucher, N. Aso, M. Nishi, H. Kageyama, and Y. Ueda, “Dzyaloshinskii-Moriya Interaction in the 2D Spin Gap System  $\text{SrCu}_2(\text{BO}_3)_2$ ,” *Phys. Rev. Lett.* **87**, 167205 (2001).
- [16] S. Miyahara and K. Ueda, “Theory of the orthogonal dimer Heisenberg spin model for  $\text{SrCu}_2(\text{BO}_3)_2$ ,” *J. Phys.: Condens. Matter* **15**, R327 (2003).
- [17] K. Kodama, S. Miyahara, M. Takigawa, M. Horvatić, C. Berthier, F. Mila, H. Kageyama, and Y. Ueda, “Field-induced effects of anisotropic magnetic interactions in  $\text{SrCu}_2(\text{BO}_3)_2$ ,” *J. Phys. Condens. Matter* **17**, L61 (2005).
- [18] Shin Miyahara and Frédéric Mila, “The Effects of Dzyaloshinsky-Moriya Interaction in the Orthogonal Dimer Heisenberg Model for  $\text{SrCu}_2(\text{BO}_3)_2$ ,” *Prog. Theor. Phys. Suppl.* **159**, 33–38 (2005).
- [19] Z. Shi, S. Dissanayake, P. Corboz, W. Steinhardt, D. Graf, D. M. Silevitch, H. A. Dabkowska, T. F. Rosenbaum, F. Mila, and S. Haravifard, “Discovery of quantum phases in the Shastry-Sutherland compound  $\text{SrCu}_2(\text{BO}_3)_2$  under extreme conditions of field and pressure,” *Nat. Commun.* **13**, 2301 (2022).
- [20] T. Waki, K. Arai, M. Takigawa, Y. Saiga, Y. Uwatoko, H. Kageyama, and Y. Ueda, “A Novel Ordered Phase in  $\text{SrCu}_2(\text{BO}_3)_2$  under High Pressure,” *J. Phys. Soc. Jpn.* **76**, 073710 (2007).
- [21] M. E. Zayed, Ch. Rüegg, J. Larrea J., A. M. Läuchli, C. Panagopoulos, S. S. Saxena, M. Ellerby, D. F. McMorrow, Th. Strässle, S. Klotz, G. Hamel, R. A. Sadykov, V. Pomjakushin, M. Boehm, M. Jiménez-Ruiz, A. Schneidewind, E. Pomjakushina, M. Stingaciu, K. Conder, and H. M. Rønnow, “4-spin plaquette singlet state in the Shastry-Sutherland compound  $\text{SrCu}_2(\text{BO}_3)_2$ ,” *Nat. Phys.* **13**, 962 (2017).
- [22] T. Sakurai, Y. Hirao, K. Hijii, S. Okubo, H. Ohta, Y. Uwatoko, K. Kudo, and Y. Koike, “Direct Observation of the Quantum Phase Transition of  $\text{SrCu}_2(\text{BO}_3)_2$  by High-Pressure and Terahertz Electron Spin Resonance,” *J. Phys. Soc. Jpn.* **87**, 033701 (2018).
- [23] J. Guo, G. Sun, B. Zhao, L. Wang, W. Hong, V. A. Sidorov, N. Ma, Q. Wu, S. Li, Z. Y. Meng, A. W. Sandvik, and L. Sun, “Quantum phases of  $\text{SrCu}_2(\text{BO}_3)_2$  from high-pressure thermodynamics,” *Phys. Rev. Lett.* **124**, 206602 (2020).
- [24] J. Larrea Jiménez, S. P. G. Crone, E. Fogh, M. E. Zayed, R. Lortz, E. Pomjakushina, K. Conder, A. M. Läuchli, L. Weber, S. Wessel, A. Honecker, B. Normand, Ch. Rüegg, P. Corboz, H. M. Rønnow, and F. Mila, “A quantum magnetic analogue to the critical point of water,” *Nature* **592**, 370–375 (2021).
- [25] and P. Wang J. Guo, C. Huang, B.-B. Chen, W. Hong, S. Cai, J. Zhao, J. Han, X. Chen, Y. Zhou, S. Li, Q. Wu, Z. Y. Meng, and L. Sun, “Deconfined quantum critical point lost in pressurized  $\text{SrCu}_2(\text{BO}_3)_2$ ,” , 2310.20128 (2023).
- [26] I. Loa, F.X. Zhang, K. Syassen, P. Lemmens, W. Crichton, H. Kageyama, and Y. Ueda, “Crystal structure and lattice dynamics of  $\text{SrCu}_2(\text{BO}_3)_2$  at high pressures,” *Physica B* **359-361**, 980–982 (2005).
- [27] S. Haravifard, A. Banerjee, J. van Wezel, D. M. Silevitch, A. M. dos Santos, J. C. Lang, E. Kermarrec, G. Srajer, B. D. Gaulin, J. J. Molaison, H. A. Dabkowska, and T. F. Rosenbaum, “Emergence of long-range order in sheets of magnetic dimers,” *Proc. Natl. Acad. Sci.* **111**, 14372–14377 (2014).
- [28] M. E. Zayed, Ch. Rüegg, E. Pomjakushina, M. Stingaciu, K. Conder, M. Hanfland, M. Merlini, and H. M. Rønnow, “Temperature dependence of the pressure induced monoclinic distortion in the spin Shastry–Sutherland compound  $\text{SrCu}_2(\text{BO}_3)_2$ ,” *Solid State Commun.* **186**, 13 (2014).
- [29] M. E. Zayed, *Novel States in Magnetic Materials under Extreme Conditions: A High Pressure Neutron Scattering Study of the Shastry-Sutherland compound  $\text{SrCu}_2(\text{BO}_3)_2$* , Ph.D. thesis, Ecole Polytechnique Fédérale de Lausanne (2010).
- [30] See Supplemental Material at [URL will be inserted by publisher], which includes Refs. [31–39], for detailed descriptions of experimental setup, analysis procedures and modelling.
- [31] H. Kageyama, K. Onizuka, T. Yamauchi, and Y. Ueda, “Crystal growth of the two-dimensional spin gap system  $\text{SrCu}_2(\text{BO}_3)_2$ ,” *J. Cryst. Growth* **206**, 65–67 (1999).
- [32] G. Jorge, M. Jaime, N. Harrison, R. Stern, H. Dabkowska, and B. D. Gaulin, “High magnetic field magnetization and specific heat of the 2D spin-dimer system  $\text{SrCu}_2(\text{BO}_3)_2$ ,” *J. Alloys Compd.* **369**, 90–92 (2004).
- [33] S. Klotz, *Techniques in High Pressure Neutron Scattering* (Taylor & Francis / CRC Press, Boca Raton, 2013).
- [34] S. Klotz, Th. Strässle, B. Lebert, M. d’Astuto, and Th. Hansen, “High pressure neutron diffraction to beyond 20 GPa and below 1.8 K using Paris-Edinburgh load frames,” *High Press. Res.* **36**, 73–78 (2016).
- [35] C. Boos, S. P. G. Crone, I. A. Niesen, P. Corboz, K. P. Schmidt, and F. Mila, “Competition between intermediate plaquette phases in  $\text{SrCu}_2(\text{BO}_3)_2$ ,” *Phys. Rev. B* **100**, 140413(R) (2019).
- [36] K. Kodama, M. Takigawa, M. Horvatić, C. Berthier, H. Kageyama, Y. Ueda, S. Miyahara, F. Becca, and F. Mila, “Magnetic superstructure in the two-dimensional quantum antiferromagnet  $\text{SrCu}_2(\text{BO}_3)_2$ ,” *Science* **298**, 395 (2002).
- [37] E. Manousakis, “The spin-1/2 Heisenberg antiferromagnet on a square lattice and its application to the cuprous oxides,” *Rev. Mod. Phys.* **94**, 1 (1991).
- [38] J. D. Reger and A. P. Young, “Monte Carlo simulations of the spin- $\frac{1}{2}$  Heisenberg antiferromagnet on a square lattice,” *Phys. Rev. B* **37**, 5978 (1988).
- [39] A. W. Sandvik, “Finite-size scaling of the ground-state parameters of the two-dimensional Heisenberg model,” *Phys. Rev. B* **56**, 11678 (1997).
- [40] K. Komatsu, S. Klotz, A. Shinzaki, R. Iizuka, L. E. Bove, and H. Kagi, “Performance of ceramic anvils for high pressure neutron scattering,” *High Press. Res.* **34**, 494–499 (2014).
- [41] S. Klotz, Th. Hansen, E. Lelièvre-Berna, L. Amand, J. Maurice, and C. Payre, “Advances in the use of Paris-Edinburgh presses for high pressure neutron scattering,” *J. Neutron Res.* **21**, 117–124 (2019).

- [42] N. P. Funnell, C. L. Bull, and C. J. Ridley, “Optimisation of toroidal ZTA anvils and gaskets; towards improved load and pressure performance,” *High Press. Res.* **41**, 306–317 (2021).
- [43] S. Toth and B. Lake, “Linear spin wave theory for single- $Q$  incommensurate magnetic structures,” *J. Phys.: Condens. Matter* **27**, 166002 (2015).
- [44] D. I. Badrtdinov, A. A. Tsirlin, V. V. Mazurenko, and F. Mila, “ $\text{SrCu}_2(\text{BO}_3)_2$  under pressure: A first-principles study,” *Phys. Rev. B* **101**, 224424 (2020).
- [45] J. B. Goodenough, “Theory of the Role of Covalence in the Perovskite-Type Manganites  $[\text{La}, M(\text{II})]\text{MnO}_3$ ,” *Phys. Rev.* **100**, 564 (1955).
- [46] J. Kanamori, “Superexchange interaction and symmetry properties of electron orbitals,” *J. Phys. Chem. Solids* **10**, 87–98 (1959).
- [47] Y. Mizuno, T. Tohyama, S. Maekawa, T. Osafune, N. Motoyama, H. Eisaki, and S. Uchida, “Electronic states and magnetic properties of edge-sharing Cu-O chains,” *Phys. Rev. B* **57**, 5326 (1998).
- [48] S. Miyahara and K. Ueda, “Thermodynamic properties of three-dimensional orthogonal dimer model for  $\text{SrCu}_2(\text{BO}_3)_2$ ,” *J. Phys. Soc. Jpn. (Suppl.) B* **69**, 72 (2000).
- [49] A. Wietek, P. Corboz, S. Wessel, B. Normand, F. Mila, and A. Honecker, “Thermodynamic properties of the Shastry-Sutherland model throughout the dimer-product phase,” *Phys. Rev. Research* **1**, 033038 (2019).
- [50] A. Koga, “Ground-State Phase Diagram for the Three-Dimensional Orthogonal-Dimer System,” *Jour. Phys. Soc. Jpn.* **69**, 3509–3512 (2000).
- [51] P. C. G. Vlaar and P. Corboz, “Tensor network study of the Shastry-Sutherland model with weak interlayer coupling,” *SciPost Phys.* **15**, 126 (2023).
- [52] J. Y. Lee, Y.-Z. You, S. Sachdev, and A. Vishwanath, “Signatures of a deconfined phase transition on the Shastry-Sutherland lattice: Applications to quantum critical  $\text{SrCu}_2(\text{BO}_3)_2$ ,” *Phys. Rev. X* **9**, 041037 (2019).
- [53] J. Yang, A. W. Sandvik, and L. Wang, “Quantum criticality and spin-liquid phase in the Shastry-Sutherland model,” *Phys. Rev. B* **105**, L060409 (2022).
- [54] Y. Cui, L. Liu, H. Lin, K.-H. Wu, W. Hong, X. Liu, C. Li, Z. Hu, N. Xi, S. Li, R. Yu, A. W. Sandvik, and W. Yu, “Proximate deconfined quantum critical point in  $\text{SrCu}_2(\text{BO}_3)_2$ ,” *Science* **380**, 1179 (2023).
- [55] C. Yasuda, S. Todo, K. Hukushima, F. Alet, M. Keller, M. Troyer, and H. Takayama, “Néel Temperature of Quasi-Low-Dimensional Heisenberg Antiferromagnets,” *Phys. Rev. Lett.* **94**, 217201 (2005).
- [56] E. Fogh, M. Boehm, G. Girit, U. B. Hansen, A. Ivanov, A. Piovano, H. M. Rønnow, I. Safiulina, J.-R. Soh, and M. E. Zayed, “Magnetic excitation spectrum at the deconfined quantum critical point of the Shastry-Sutherland compound,  $\text{SrCu}_2(\text{BO}_3)_2$ ,” (2021), doi:10.5291/ILL-DATA.4-01-1655.
- [57] E. Fogh, M. Boehm, G. Girit, A. Piovano, H. M. Rønnow, and M. E. Zayed, “The Néel phase in the Shastry-Sutherland compound  $\text{SrCu}_2(\text{BO}_3)_2$ ,” (2021), doi:10.5291/ILL-DATA.DIR-258.

## Supplemental Material to accompany the article

### Spin Waves and Three Dimensionality in the High-Pressure Antiferromagnetic Phase of $\text{SrCu}_2(\text{BO}_3)_2$

Ellen Fogh, Gaétan Girit, Mohamed E. Zayed, Andrea Piovano, Martin Boehm, Paul Steffens, Irina Safiulina, Ursula B. Hansen, Stefan Klotz, Jian-Rui Soh, Ekaterina Pomjakushina, Frédéric Mila, Bruce Normand, and Henrik M. Rønnow

#### S1. INELASTIC NEUTRON SCATTERING UNDER HIGH PRESSURE

##### A. Single-crystal sample

The disk-shaped single-crystalline sample was cut from a large crystal grown by the floating-zone method [1, 2]. Single-crystal diffraction measurement on samples taken from the same batch confirmed the good quality of these crystals, namely that the structure is well ordered, with no observable signatures of twinning or impurities. The calculated bond valence sums were within 10% of the expected valence. The sample used for pressurization, shown in Fig. S1(a), had a diameter of 4 mm, thickness 1.3 mm, and total weight 58 mg, and was mounted with  $(q_h, q_k, 0)$  oriented in the horizontal scattering plane [Fig. S1(c)].

##### B. Pressure-cell loading procedure

Inelastic neutron scattering (INS) remains the only experimental probe in the field of quantum magnetism that delivers fully momentum-resolved spectral information. However, the requirement for large samples makes the combination with high pressures and low temperatures a significant challenge. Nevertheless, recent developments in high-pressure techniques at the Institute Laue-Langevin enabled us to perform INS measurements under the required pressures on the triple-axis spectrometers IN8 and ThALES [3–5].

The sample was inserted in a TiZr gasket held together with a TiZr ring and deuterated 4:1 methanol-ethanol was used as the pressure medium [Fig. S1(b)]. The TiZr alloy produces almost zero scattering and therefore provides a very clean background both for diffraction and for inelastic measurements. The assembly was placed between zirconia-toughened alumina anvils with a single-toroidal profile [3, 5, 6] in a steel clamp, which was then inserted in the Paris-Edinburgh (PE) press. Pressure was applied in the capillary via the He gas-handling system and the load curve was followed to a final capillary pressure of 1111 bar (which corresponds to a load of 73 tonnes on the anvils). The pressure on the sample was increased in steps corresponding to approximately 1 GPa at room temperature, and its relation with the capillary pressure is discussed in Sec. S1D. Initial cooling of the system to around 80 K was assisted by liquid  $\text{N}_2$  in the sample

chamber. The  $\text{N}_2$  was subsequently pumped out and the closed-cycle refrigerator then took the system to 4.5 K. The total duration of the cooling procedure from room to base temperature was approximately 6 hours.

##### C. Scattering geometry in real and reciprocal space

Measurements on IN8 were performed with fixed  $k_f = 2.66 \text{ \AA}^{-1}$ , using a PG(002) analyzer and a PG filter between sample and analyzer to suppress higher harmonics. The incoming energy was selected by a Si(111) monochromator. Both monochromator and analyzer were focused in order to maximize the neutron flux on the sample. To lower the overall background neutron counts, slits were placed both before and after the sample position to limit the illuminated area, as well as to limit the locations from which scattered neutrons could reach the detector. The opening sizes were 18 (16) cm horizontally and 30 (40) cm vertically on the incoming (outgoing) beam. No collimation was used because the Cd-coated PE cell effectively collimates the beam, allowing a beam divergence of approximately  $60^\circ$ , depending on the opening between the anvils. The instrument configuration used on ThALES was very similar to that on IN8, except for the lower neutron energy (fixed  $k_f = 1.50 \text{ \AA}^{-1}$ ), which provided a better resolution (Sec. S1E). PG(002) was used for both monochromator and analyzer on ThALES.

The accessible volume in momentum transfer,  $\mathbf{Q}$ , and energy transfer,  $E$ , is limited by the support pillars of the PE press, as well as by the usual geometrical and kinematic constraints of a triple-axis spectrometer. By considering these limitations, we found that the optimal coverage in  $\mathbf{Q}$  is obtained when the sample is oriented with  $(0, 1, 0)$  in the direction of the pillar. An example of the scattering geometry in real space is shown in Fig. S1(c).

##### D. Pressure determination

The actual pressure applied in our experiment was determined from the lattice constant of  $\text{SrCu}_2(\text{BO}_3)_2$ , which has been measured as a function of pressure at room temperature [7]. We base our notation on the conventions of triple-axis spectrometry, which depends on six angles, two for each axis, named  $a_i$  with  $i = 1, \dots, 6$ . Of these, the most important for the physics of the sample



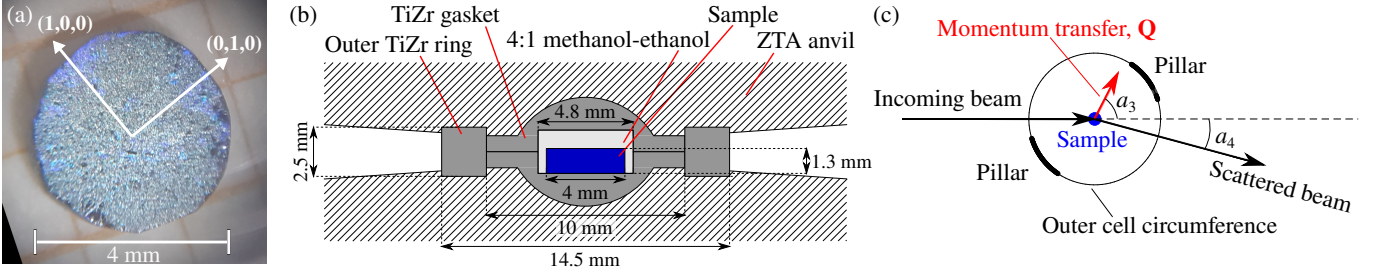


FIG. S1. (a)  $\text{SrCu}_2(\text{BO}_3)_2$  single crystal used for high-pressure neutron scattering experiments. (b) Schematic representation of the sample and gasket assembly (not to scale). (c) Scattering geometry illustrating the positions of the support pillars of the Paris-Edinburgh (PE) press. This configuration represents the IN8 experiment, where  $k_f = 2.66 \text{ \AA}^{-1}$  and the sample was oriented with  $(0, 1, 0)$  in the direction of the pillar. Specifically shown here, the conditions  $\mathbf{Q} = (-0.5, 1, 0)$  and  $\Delta E = 3 \text{ meV}$  leave both the incoming and outgoing beam paths clear.

are the angles  $a_3$  and  $a_4$ , where the scattering angle,  $a_4$ , is the analog of  $2\theta$  in a diffraction experiment. To obtain a reference point at ambient temperature and pressure,  $a_4$  scans were performed for 4 sets of Friedel pairs of accessible nuclear Bragg peaks [i.e.  $(q_h, q_k, q_l)$  and  $(\bar{q}_h, \bar{q}_k, \bar{q}_l)$ ] and the positions fitted to the expression

$$a_4 = -2 \sin^{-1} \left( \frac{\pi \sqrt{q_h^2 + q_k^2}}{ka(0)} \right) + \Delta a_4 + q_h \phi + q_k \phi', \quad (\text{S1})$$

where the fitted variables are the ambient-pressure lattice constant,  $a(0)$ , the instrumental scattering-angle offset,  $\Delta a_4$ , and angles  $\phi$  and  $\phi'$ , which are both functions of  $a_3$  and  $a_4$  and represent offsets in sample rotation, out-of-plane tilt, and off-center sample position. We applied Eq. (S1) using both the fitted  $a_4$  positions obtained from these scans and those defined by the center of mass of the measured neutron intensities. Turning to finite pressures,  $a_4$  scans for the  $(0, 4, 0)$  nuclear peak at different capillary pressures are shown in Fig. S2(a). Performing such a scan at the highest pressure and using  $P = \frac{1}{\alpha} \left( 1 - \frac{a(P)}{a(0)} \right)$ , where  $\alpha = 1.319(6) \times 10^{-3} \text{ GPa}^{-1}$  from Ref. [7], we obtain a pressure of 5.9(5) GPa both when using center-of-mass peak positions and fitted peak positions. These estimates are in agreement with the nominal pressure of 5.5 GPa given by the load curve of the PE press. Figure S2(b) shows the relative change in lattice constant and the corresponding pressures determined by these different approaches as a function of capillary pressure. Because the data at the highest pressure was measured at 25 K, we also took into account the thermal expansion as measured at ambient pressure [inset Fig. S2(b)].

The in-plane structure of  $\text{SrCu}_2(\text{BO}_3)_2$  is very stiff, which manifests itself as a relatively large uncertainty (approximately 0.5 GPa) in the pressure determination. We note also that the in-plane compression remains linear despite the system going through a structural transition. The small splitting between the in-plane lattice constants,  $a(P)$  and  $b(P)$ , observed in Ref. [7] is too small (below 1% even at 5.5 GPa) to be detected in our experiment. We therefore neglect the monoclinic structure for

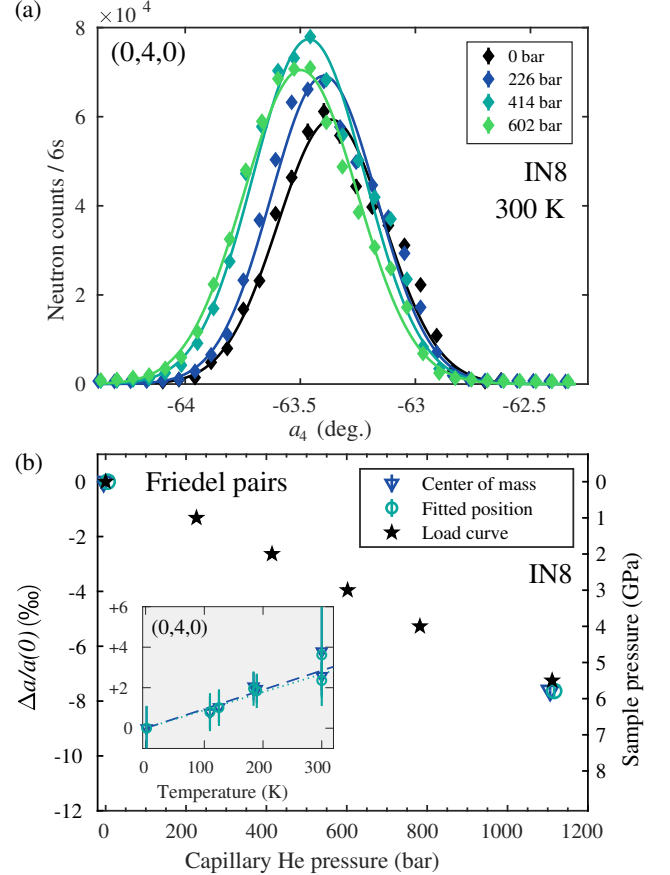


FIG. S2. (a) Shift of the  $(0, 4, 0)$  nuclear Bragg peak toward larger scattering angles with increasing capillary He pressure. (b) Pressure determination from the change in the lattice constant of  $\text{SrCu}_2(\text{BO}_3)_2$ , shown as a function of the capillary He pressure. Neutron data (triangles and circles) were acquired at 25 K but corrected for thermal expansion to 300 K for comparison with the load curve (stars). The inset shows the corresponding thermal expansion upon heating at ambient pressure.

the purpose of estimating the pressure and retain the tetragonal notation throughout our manuscript.

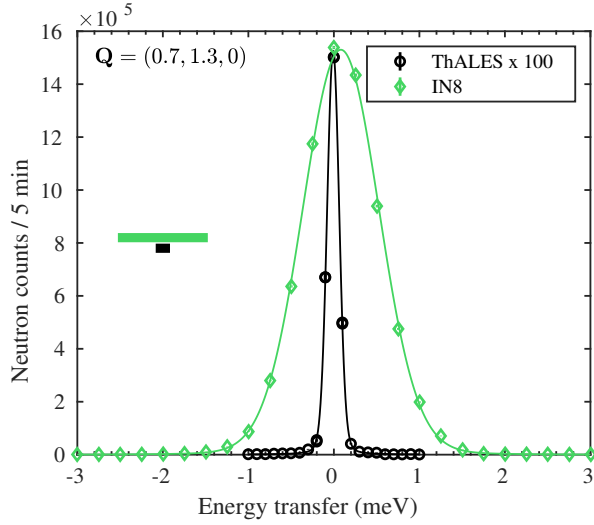


FIG. S3. Neutron counts measured at ThALES and IN8 as a function of energy transfer at  $\mathbf{Q} = (0.7, 1.3, 0)$ . Full-width half-maximum heights determined by fits to a pseudo-Voigt function are shown as the horizontal bars and attain respective values of 0.167(4) and 1.05(1) meV for the two instruments when measuring with  $k_f = 1.5$  and  $k_f = 2.66 \text{ \AA}^{-1}$ .

### E. Data treatment

The neutron intensities,  $I(q_k)$ , collected at constant energy transfer and as a function of  $q_k$  in  $(0, q_k, 0)$  were fitted to the expression

$$I(q_k) = I_1^- e^{-[q_k - (1 - \delta_k)]^2 / 2\sigma^2} + I_1^+ e^{-[q_k - (1 + \delta_k)]^2 / 2\sigma^2} + I_3^- e^{-[q_k - (3 - \delta_k)]^2 / 2\sigma^2} + I_3^+ e^{-[q_k - (3 + \delta_k)]^2 / 2\sigma^2} + A q_k + B, \quad (\text{S2})$$

where  $I_1^\pm$  and  $I_3^\pm$  are the individual peak intensities,  $\delta_k$  is the displacement of the mode with respect to either  $(0, 1, 0)$  or  $(0, 3, 0)$ ,  $\sigma$  is the Gaussian peak width, and  $A$  and  $B$  define a linear background. The intensities,  $I(q_h)$ , measured along  $(q_h, 1, 0)$  were described by a similar expression but with two different mode displacements, respectively  $\delta_h$  and  $\delta'_h$  from  $(0, 1, 0)$  and  $(1, 1, 0)$ . All intensities were forced to have positive definite values. To account for the additional scattering contributions above the minimum of the spin-wave dispersion evident in Fig. 3(a) and 3(b) of the main text, as well as for resolution effects, the fitting procedure was constrained manually to capture the onset of neutron intensity in  $\mathbf{Q}$  [Figs. 2(a) and 2(b) of the main text]. We comment that we did not consider any phonon contributions to the measured signal, because, in line with previous INS experiments on  $\text{SrCu}_2(\text{BO}_3)_2$  at lower pressures, no unexpected sharp features were observed that required further investigation.

For measurements performed at constant momentum transfer as a function of energy, determining peak positions close to the elastic line requires knowledge of the in-

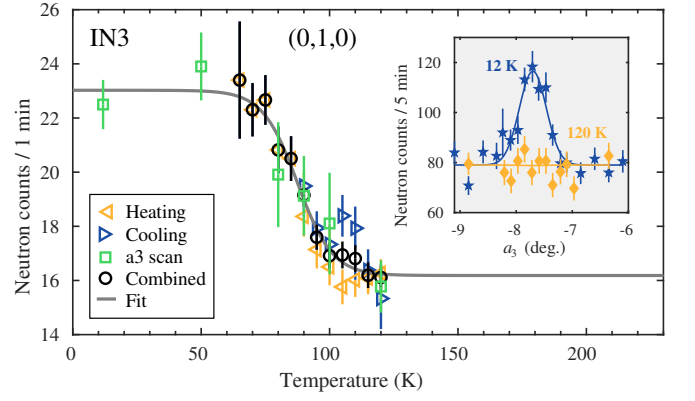


FIG. S4. Peak intensity of the  $(0, 1, 0)$  magnetic Bragg peak measured on IN3 as a function of temperature. Data collected while ramping the temperature (both heating and cooling) are binned into 5 K intervals. The gray line shows the fit described in the text. The inset shows full rocking curves at 12 and 120 K.

coherent scattering contribution. Figure S3 shows scans across zero energy transfer collected on both IN8 and ThALES at  $\mathbf{Q} = (0.7, 1.3, 0)$ , a position where no inelastic or diffraction signal is expected and therefore this measurement represents the incoherent scattering. Using a pseudo-Voigt function to fit the line shapes yielded the quoted energy resolutions on both instruments. The incoherent contribution to the spectra in Fig. 2(d) of the main text was scaled to the  $\mathbf{Q}$ -dependent neutron intensity at zero energy transfer, and one or two Gaussians were then fitted to determine the mode positions.

### F. IN3 experiment and diffraction results

Supporting diffraction data were collected at ThALES with the same loading used for our INS measurements, and more detailed diffraction measurements were carried out later on IN3 (also at the Institute Laue-Langevin). For this experiment, a second pressure-cell loading was prepared by following the procedure described in Sec. S1B to obtain 5.5 GPa at the sample position. The incoming and outgoing energies were fixed for diffraction ( $k_i = k_f = 2.66 \text{ \AA}^{-1}$ ) and the base temperature was 12 K.

In Fig. S4 we study the intensity of the  $(0, 1, 0)$  magnetic Bragg peak, showing data obtained both by counting on the peak position while ramping the temperature up or down and by fitting Gaussian peaks to full rocking scans collected after stabilizing the temperature (inset; the rocking curve is obtained by varying  $a_3$ , which is the analog of  $\omega$  in diffraction). Because the temperature is measured at the bottom of the PE cell, the actual sample temperature may lag significantly behind the reading obtained while ramping. This effect would manifest as hysteresis in the intensity between heating and cooling. However, by sufficiently slow ramping we eliminated any

hysteresis and our combined (heating and cooling) data agreed well with the results from rocking scans.

The physics of the thermal evolution shown in Fig. S4 remains open to interpretation. Here we apply a phenomenological fit to the neutron intensity of the form  $I(T) = I_0 \tanh(\beta(T_N - T)) + C$ , where  $I_0$  is a scale factor and  $C$  a constant background. In this expression, the thermal transition is a gradual process whose width is expressed by  $\beta$  and the transition temperature,  $T_N$ , is determined from the steepest point on the intensity curve in Fig. S4. From this procedure we obtain  $T_N = 88(2)$  K, a number lower than the previously reported values around 120 K [8, 9]. This latter temperature is more appropriate for describing the onset of intensity in our IN3 data, which indicate a more gradual transition than the power-law onset suggested earlier. These discrepancies may be explained by differences in the pressure determination and also, based on the long lag times we observe in attaining thermal equilibrium, by the possibility of insufficient temperature control in the previous studies. Although our pressure estimate is subject to a relatively large uncertainty, the appearance of the  $(0, 1, 0)$  magnetic Bragg peak below  $T_N$  places our measurement clearly in the monoclinic and antiferromagnetic part of the phase diagram, and the observation of spin waves provides unambiguous support for this conclusion.

On ThALES we also collected rocking curves around the  $(0, 1, 0)$  magnetic Bragg peak at temperatures of 12, 5, and 1.5 K. The temperature of 1.5 K was obtained by filling liquid He into the sample chamber and subsequently pumping following the procedure described in Ref. [10]. The fact that we observe no changes in behavior within this temperature interval suggests that the feature observed in the specific heat around 8 K [11] is not of a type that could manifest itself in neutron diffraction.

## S2. SPIN-WAVE MODELING

To interpret the spectra of  $\text{SrCu}_2(\text{BO}_3)_2$  observed by high-pressure INS, we use linear spin-wave theory with assistance from the `spinW` package [12] to calculate matching dispersion relations. Because the crystal symmetry changes from tetragonal to monoclinic above 4 GPa, a complete model should in principle consider inequivalent in-plane magnetic interactions arising from the inequivalent superexchange paths, namely intradimer interactions  $J_1$  and  $J_2$  and interdimer interactions  $J'_1$  and  $J'_2$  [13]. The change of symmetry should also lead to a doubling in the number of DM interactions, as well as to a possible enhancement of their values. Faced with this plethora of candidate parameters, we adopt the approach of finding a minimal model. Motivated by the very small breaking of tetragonal symmetry in the monoclinic structure, we begin by retaining only the SSM (i.e. interactions  $J$  and  $J'$ ) in the plane, and then add as few qualitatively different interactions as possible, verify-

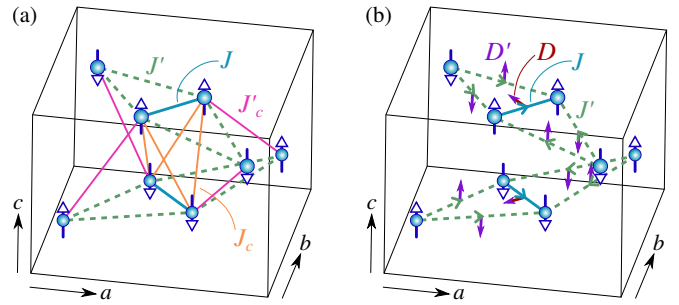


FIG. S5. Schematic illustration of (a) interlayer and (b) DM interactions considered in modeling the spin-wave dispersion.

ing *post facto* whether the model captures satisfactorily the observed features of the spin-wave spectrum.

In the AFM phase of the SSM, the dimer spins are forced into a parallel configuration, as illustrated in Fig. S5. The spin-wave spectrum of this model contains a Goldstone mode and an optical branch, both of which are doubly degenerate for the unit cell of  $\text{SrCu}_2(\text{BO}_3)_2$ . More elements are therefore required to explain the measured spectra (Figs. 2-3 of the main text), and in the following we illustrate the effects of additional interlayer Heisenberg and intralayer DM interactions.

### A. Effect of interlayer interactions

By inspection of the superexchange paths, there are two candidate interlayer interactions in  $\text{SrCu}_2(\text{BO}_3)_2$  [Fig. S5(a)], the bond  $J_c$  between orthogonal dimers illustrated in Fig. 1(c) of the main text and the bond  $J'_c$  between parallel dimers offset by one diagonal plaquette spacing. The effect of both is to lift the degeneracy between the lower modes in the dispersion such that one branch remains the Goldstone mode and the other is raised to a finite value, as shown in Fig. S6(a). The orthogonal arrangement of the dimers generates a characteristic structure factor, with the intensity of the Goldstone mode vanishing at  $(0, 1, 0)$  while the gapped mode has maximum intensity, and vice versa at  $(1, 1, 0)$ . This behavior occurs only for  $J_c > 0$  (AFM) and  $J'_c < 0$  (FM), and is inverted if these signs are exchanged. Because a FM interaction is unlikely for a bond with the geometry of  $J'_c$  [Fig. S5(a)], we do not consider this term further. The vanishing of the Goldstone mode leads to the appearance that a gap has opened at  $(0, 1, 0)$ , but not at  $(1, 1, 0)$ , while at  $(0, 2, 0)$  only the upper branches have any intensity.

The size of the Goldstone-mode splitting,  $\Delta = 8S\sqrt{J'J_c}$ , is determined only by  $J_c$ , and is not sensitive to the level of frustration,  $J/J'$ , as we show in Figs. S6(b) and S6(d). This situation allows for a precise estimate of the interlayer coupling directly from the measured value  $\Delta = 1.9$  meV; the result we obtain,  $J_c = 0.053(3)$  meV, is surprisingly small, given its strong effect on the spectrum, but this is explained by the square-root dependence of

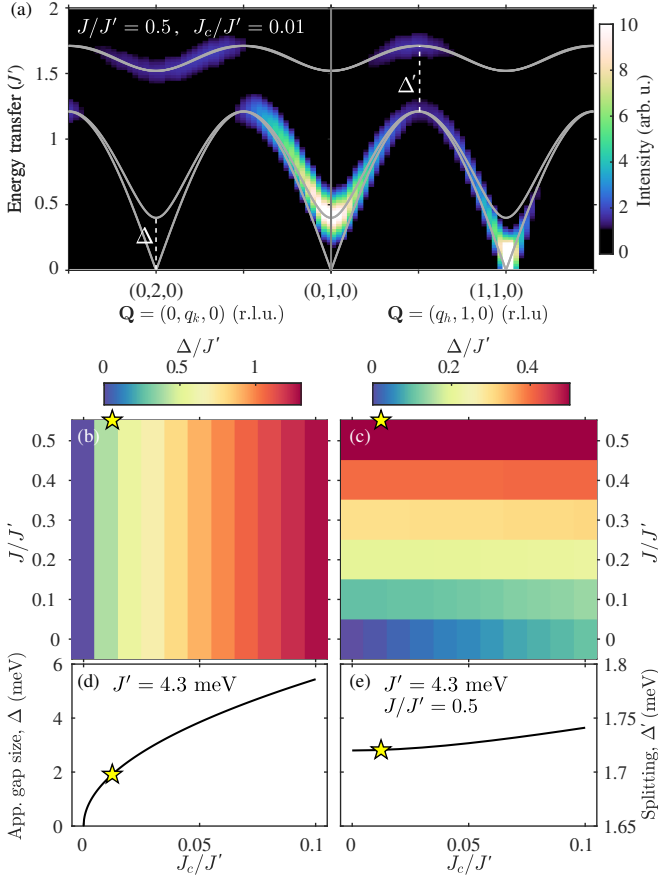


FIG. S6. Effects of interlayer coupling on the spin-wave dispersion. (a) Spectrum calculated for  $J/J' = 0.5$  and  $J_c/J' = 0.01$ , with the Goldstone-mode splitting at  $(0, 1, 0)$ ,  $\Delta$ , and the splitting between upper and lower branches at  $(0.5, 1, 0)$ ,  $\Delta'$ , indicated by vertical dashed lines. Gray lines show the mode positions and color contours the calculated neutron intensities. (b),(c) Values of  $\Delta$  and  $\Delta'$  shown as functions of the SSM frustration,  $J/J'$ , and the interlayer coupling,  $J_c$ . (d)  $\Delta$  as a function of  $J_c/J'$  at fixed  $J' = 4.3$  meV, showing a clear square-root dependence;  $\Delta$  does not depend on  $J$ . (e)  $\Delta'$  as a function of  $J_c/J'$  at fixed  $J' = 4.3$  meV and  $J/J' = 0.5$ . The stars mark the position in parameter space determined for  $\text{SrCu}_2(\text{BO}_3)_2$ .

$\Delta$ . The splitting between upper and lower branches at  $(0.5, 1, 0)$  is given for small  $J_c$  by  $\Delta' \approx 2SJ$ , as we show in Figs. S6(c) and S6(e), and thus  $\Delta'$  offers a means of fitting the frustration ratio,  $J/J'$ . However, the very low neutron intensities in the upper branch limit the accuracy of this method. Beyond the splitting,  $J$  also reduces the overall energy scale of the lower branches, which is otherwise determined by  $J'$ . This is a common consequence of frustration, and its effect in high-pressure  $\text{SrCu}_2(\text{BO}_3)_2$ , which we illustrate in Fig. S8, was more important in our determination of  $J = 2.36(26)$  meV.

Due to the buckling of the  $\text{Cu}(\text{BO}_3)$  planes, there are in fact two inequivalent  $J_c$  bonds connecting orthogonal dimers along the  $c$  direction, which we label  $J_{c1}$  and  $J_{c2}$  and show in Fig. S9(a). To understand the consequences

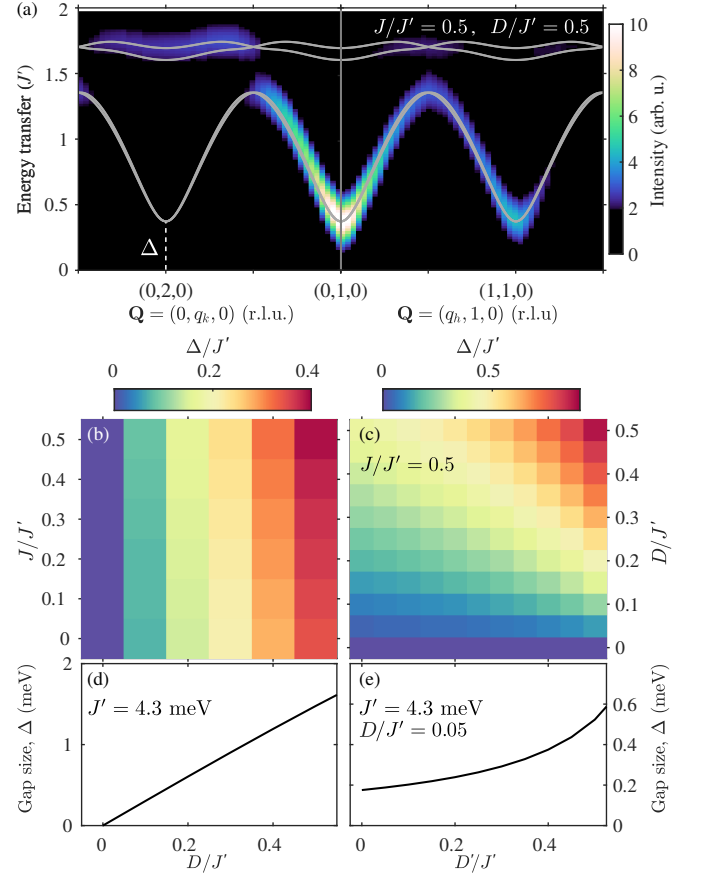


FIG. S7. Effects of DM interactions on the spin-wave dispersion. (a) Spectrum calculated for  $J/J' = 0.5$ , where a finite  $D$  produces the same real gap,  $\Delta$ , at  $(0, 1, 0)$  and  $(1, 1, 0)$ . Gray lines show the mode positions and color contours the calculated neutron intensities for  $D/J' = 0.5$ . (b),(c) Values of  $\Delta$  shown as a function of the SSM frustration,  $J/J'$ , and the two DM interaction parameters,  $D$  and  $D'$ . (d)  $\Delta$  as a function of  $D/J'$  at fixed  $J' = 4.3$  meV, showing a linear dependence. (e)  $\Delta$  as a function of  $D'/J'$  at fixed  $J' = 4.3$  meV and  $D/J' = 0.05$ .

of this situation, we include both parameters in the model and fit the INS data by fixing one while letting the other vary. We also left  $J'$  and  $J$  free, finding that the best fits were always obtained with values around  $J' = 4.3$  meV and  $J/J' = 0.5$ . The results for  $J_{c1}$  and  $J_{c2}$ , shown in Fig. S9(b), display a direct linear relationship ( $J_{c1} = -1.00(5)J_{c2} + 0.105(3)$  meV). Thus the only quantity that can be determined independently is the sum  $J_{c1} + J_{c2} = 2J_c$ , and using the single value  $J_c$  that represents the average of  $J_{c1}$  and  $J_{c2}$  is a valid procedure to follow.

## B. Effect of Dzyaloshinskii-Moriya interactions

The DM interactions in  $\text{SrCu}_2(\text{BO}_3)_2$  are generally agreed to be adequately represented by an intradimer term,  $D$ , and an interdimer term,  $D'$ , both with 3% of



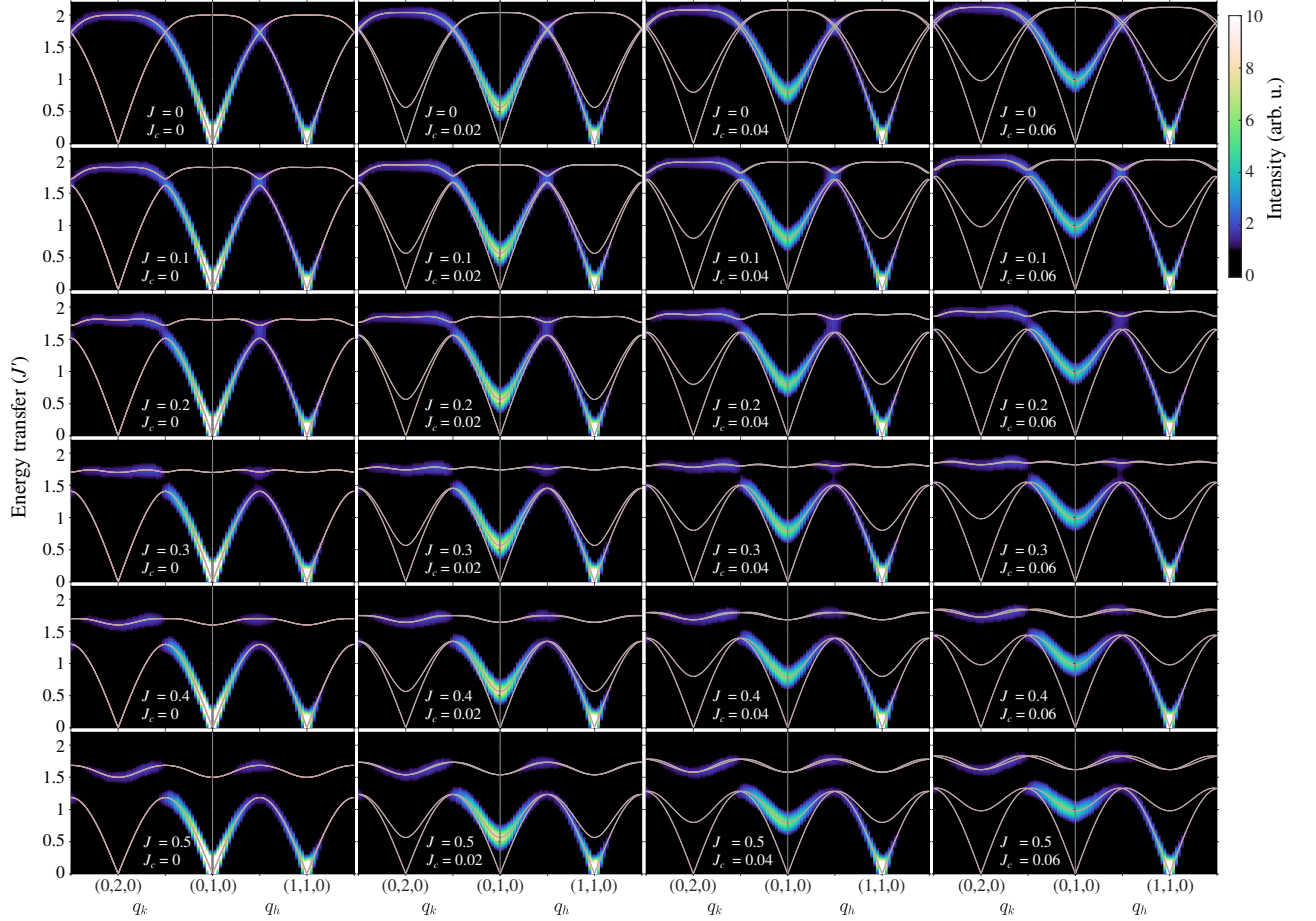


FIG. S8. Spectra calculated for  $\text{SrCu}_2(\text{BO}_3)_2$  along the directions  $\mathbf{Q} = (0, q_k, 0)$  and  $\mathbf{Q} = (q_h, 1, 0)$  that illustrate the roles of  $J$  and  $J_c$  in determining the characteristics of the dispersion.  $J/J'$  increases from top to bottom and  $J_c/J'$  from left to right. Gray lines show the mode positions and color contours the calculated neutron intensities. The splitting  $\Delta$  of the lower branch at  $(0, 1, 0)$  is controlled by  $J_c$  and the splitting  $\Delta'$  between the upper and lower branches at  $(0.5, 1, 0)$  is controlled by  $J$ .

the values of the corresponding Heisenberg interaction, i.e.  $D = 0.24$  meV and  $D' = -0.14$  meV [15], with the geometries shown in Fig. S5(b).  $D$  acts to open a real gap at all magnetic Bragg peak positions such as  $(0, 1, 0)$  and  $(1, 1, 0)$ , whereas  $D'$  on its own does not. The effects of  $D$  and  $D'$  on the spectrum are represented in Fig. S7. The DM-induced gap is nearly independent of  $J/J'$  and the linear dependence of  $\Delta$  on  $D$  means that a DM value approaching 3 meV is needed to obtain the observed gap of 1.9 meV [Fig. S7(d)]. In addition to this unrealistically large value, the requirement of that the gaps be equal at  $(0, 1, 0)$  and  $(1, 1, 0)$  [Fig. S7(a)] makes it very difficult to achieve a reasonable fit to the INS data [Figs. 3(a) and 3(b) of the main text]. While  $D$  and  $D'$  together can alter the values of these gaps, we consider DM interactions alone as a highly improbable mechanism for explaining the  $\text{SrCu}_2(\text{BO}_3)_2$  spectrum. We stress again the point made in the main text that we are not stating that the DM interactions determined in  $\text{SrCu}_2(\text{BO}_3)_2$  at ambient pressure have disappeared in the high-pressure phase: our statement is that, given the linear effects of  $D$  and  $D'$  visible in Fig. S7, it is simply not possible to

determine the presence of DM interactions below 10% of  $J'$  on the basis of our present experiment.

Given that the geometry of the intradimer bond ( $J$ ) is little changed under pressure, we do not expect the value of  $D$  to increase significantly in the monoclinic phase, even if it becomes a larger fraction of the strongly suppressed  $J$ . As noted in the main text, the  $J'$  bond becomes less symmetrical in the monoclinic phase, which may lead to an enhancement of  $D'$ , but there is no reason to expect an order-of-magnitude increase. Thus we find it reasonable to work with a minimal model in which the DM interactions have no role, but look forward to a new generation of high-pressure experiments whose accuracy makes it possible to distinguish their effects.

### C. Validity of linear spin-wave theory

In order to apply linear spin-wave theory in the AFM phase of the SSM, one would wish to verify that quantum fluctuation effects arising from the mutual frustra-

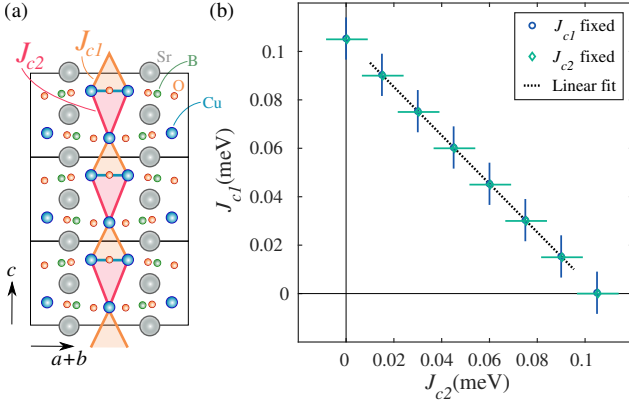


FIG. S9. (a) Projection of several unit cells along  $c$  onto one of the dimer axes to illustrate that there are two different interlayer interactions,  $J_{c1}$  (shorter bond) and  $J_{c2}$  (longer bond). (b) Results from fitting the INS data to a model with two interlayer interactions. The dotted line is a linear fit to the refined parameters.

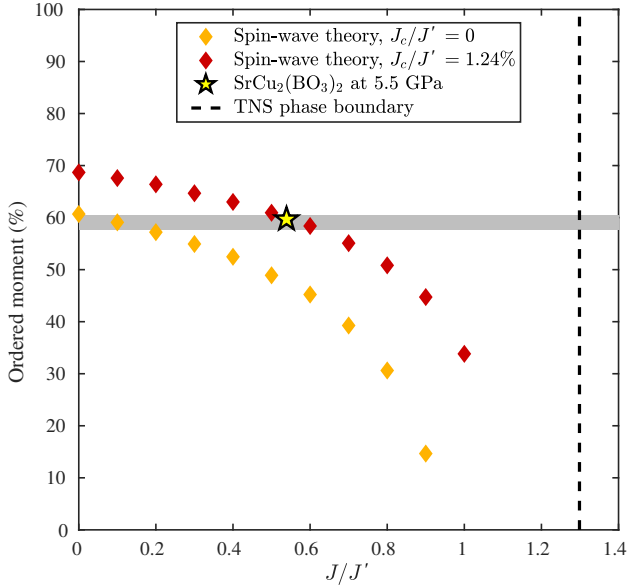


FIG. S10. Ordered moment calculated within linear spin-wave theory for the AFM phase of the SSM as a function of  $J/J'$ . Yellow diamonds show the ordered moment of the 2D system ( $J_c = 0$ ) and red diamonds the ordered moment with the experimentally determined interlayer coupling,  $J_c/J' = 0.0124$ . The star marks the moment computed with the model parameters determined for  $\text{SrCu}_2(\text{BO}_3)_2$  at 5.5 GPa. The horizontal gray line shows the result established for the nearest-neighbor square-lattice Heisenberg antiferromagnet ( $J = 0$ ,  $J_c = 0$ ). The vertical dashed line marks the phase boundary to the plaquette phase determined by numerical methods [14].

tion of  $J$  and  $J'$  do not invalidate the spin-wave framework. For this we use the `spinW` package [12] to compute the reduction of the ordered AFM moment as  $J/J'$  is increased, and show the results in Fig. S10. With  $J_c = 0$  we observe a systematic suppression of the or-

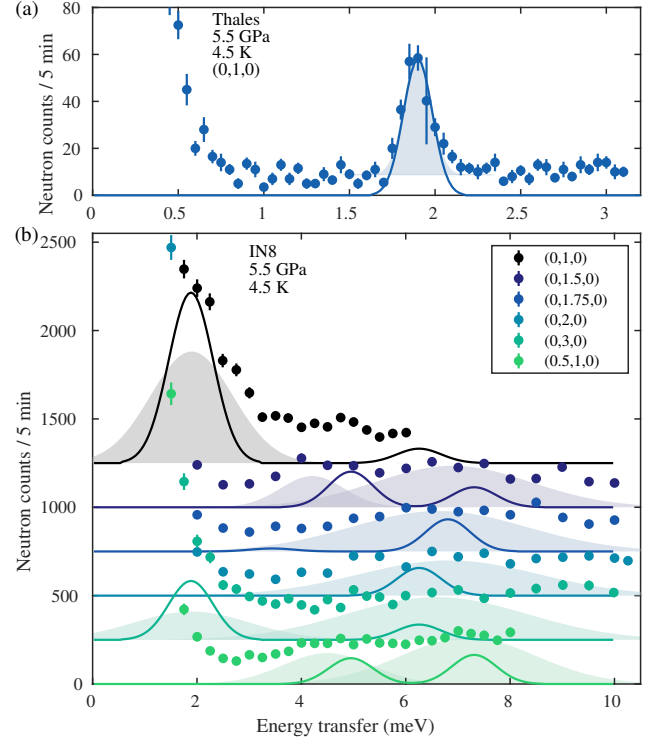


FIG. S11. INS data obtained by constant- $\mathbf{Q}$  scans performed at 5.5 GPa on ThALES (a) and on IN8 (b). In these adapted versions of Figs. 2(c) and 2(d) of the main text, the colored areas continue to represent Gaussian fits to the data (solid symbols). The solid lines were obtained by placing  $\delta$ -functions at the mode positions predicted by our global spin-wave fit and convolving these with energy resolutions of 0.2 meV for the ThALES data and 1.0 meV for the IN8 data. The intensity difference between the lines and the data may be taken as an estimate of the additional scattering contributions lying beyond linear spin-wave theory.

dered moment until the calculation becomes unstable near  $J/J' = 1$ . However,  $\text{SrCu}_2(\text{BO}_3)_2$  at 5.5 GPa is not far from the  $J = 0$  limit, where the linear spin-wave calculation matches rather well the 61% order familiar from the nearest-neighbor square-lattice Heisenberg antiferromagnet [16–18]. When the small interlayer coupling determined for high-pressure  $\text{SrCu}_2(\text{BO}_3)_2$  is included, the ordered moment is enhanced quite substantially [Fig. S10] and we obtain a value of 59.7%, which justifies the application of linear spin-wave theory.

Nevertheless, the square-lattice model does have some very well documented departures from linear spin-wave theory, particularly for energies at and above the zone-boundary energy of the single spin wave, and these can be expected to play a role in the weak but complex scattered intensity profile we find in the region of the two optical spin-wave branches. Beyond the renormalization factor,  $Z_c$ , mentioned in the main text, which would alter the one-magnon branch energies (and hence the estimated  $J$  and  $J'$  values) by approximately 20%, the spectrum of a frustrated quantum square-lattice system should show

a weak two-magnon scattering continuum arising from two unbound acoustic magnons. The physics of the SSM in the dimer and plaquette phases is dominated by two-magnon bound states favored by the very strong frustration, and even at the weaker frustration we find in the monoclinic phase, a detailed calculation of possible magnon binding effects is required. Finally, the unfrustrated square-lattice Heisenberg antiferromagnet also shows differential renormalization of the one-magnon energies on the zone boundary and the  $(\pi, 0)$  scattering anomaly (ascribed by different authors to magnon fractionalization and to bound-state formation), and these quantum many-body effects are expected to be stronger in the presence of additional frustration.

While we cannot determine which of these contributions are detectable around the optical magnon branches in our minimal model, their possible presence may explain why the signal in this region is very broadly distributed. For the purposes of our present data analysis, we have ascribed all of the weak intensity we observe

to the optical magnon branches. However, our fitting procedure is dominated by the acoustic branches, and this leads to two important remarks. First, the separation of the acoustic and optical branches,  $\Delta'$ , is a key parameter in our determination of the frustration ratio  $J'/J$ ; we stress that the goodness of our  $J$  fit is dictated primarily by optimizing the upper edge of the acoustic magnon branches, meaning around the points  $(0.5, 1, 0)$ ,  $(0, 1.5, 0)$ , and  $(0, 2.5, 0)$  in Fig. 3 of the main text. Second, with the optical branches constrained in this way, one may compare their intensity contribution with the total measured intensity to obtain a qualitative impression of the additional scattering arising from two-magnon contributions and other quantum fluctuation effects. As we show in Fig. S11, the predicted optical branches contribute on the order of half the measured intensity, at energies in reasonable correspondence with the observed maxima, and do leave a significant amount of scattered intensity over a broad range of energies whose explanation requires processes lying beyond linear spin-wave theory.

- 
- [1] H. Kageyama, K. Onizuka, T. Yamauchi, and Y. Ueda, “Crystal growth of the two-dimensional spin gap system  $\text{SrCu}_2(\text{BO}_3)_2$ ,” *J. Cryst. Growth* **206**, 65–67 (1999).
  - [2] G. Jorge, M. Jaime, N. Harrison, R. Stern, H. Dabkowska, and B. D. Gaulin, “High magnetic field magnetization and specific heat of the 2D spin-dimer system  $\text{SrCu}_2(\text{BO}_3)_2$ ,” *J. Alloys Compd.* **369**, 90–92 (2004).
  - [3] K. Komatsu, S. Klotz, A. Shinozaki, R. Iizuka, L. E. Bove, and H. Kagi, “Performance of ceramic anvils for high pressure neutron scattering,” *High Press. Res.* **34**, 494–499 (2014).
  - [4] S. Klotz, Th. Hansen, E. Lelièvre-Berna, L. Amand, J. Maurice, and C. Payre, “Advances in the use of Paris-Edinburgh presses for high pressure neutron scattering,” *J. Neutron Res.* **21**, 117–124 (2019).
  - [5] N. P. Funnell, C. L. Bull, and C. J. Ridley, “Optimisation of toroidal ZTA anvils and gaskets; towards improved load and pressure performance,” *High Press. Res.* **41**, 306–317 (2021).
  - [6] S. Klotz, *Techniques in High Pressure Neutron Scattering* (Taylor & Francis / CRC Press, Boca Raton, 2013).
  - [7] I. Loa, F.X. Zhang, K. Syassen, P. Lemmens, W. Crichton, H. Kageyama, and Y. Ueda, “Crystal structure and lattice dynamics of  $\text{SrCu}_2(\text{BO}_3)_2$  at high pressures,” *Physica B* **359–361**, 980–982 (2005).
  - [8] S. Haravifard, A. Banerjee, J. van Wezel, D. M. Silevitch, A. M. dos Santos, J. C. Lang, E. Kermarrec, G. Srajer, B. D. Gaulin, J. J. Molaison, H. A. Dabkowska, and T. F. Rosenbaum, “Emergence of long-range order in sheets of magnetic dimers,” *Proc. Natl. Acad. Sci.* **111**, 14372–14377 (2014).
  - [9] M. E. Zayed, Ch. Rüegg, J. Larrea J., A. M. Läuchli, C. Panagopoulos, S. S. Saxena, M. Ellerby, D. F. McMorrow, Th. Strässle, S. Klotz, G. Hamel, R. A. Sadykov, V. Pomjakushin, M. Boehm, M. Jiménez-Ruiz, A. Schneidewind, E. Pomjakushina, M. Stinaciu, K. Conder, and H. M. Rønnow, “4-spin plaquette singlet state in the Shastry-Sutherland compound  $\text{SrCu}_2(\text{BO}_3)_2$ ,” *Nat. Phys.* **13**, 962 (2017).
  - [10] S. Klotz, Th. Strässle, B. Lebert, M. d’Astuto, and Th. Hansen, “High pressure neutron diffraction to beyond 20 GPa and below 1.8 K using Paris-Edinburgh load frames,” *High Press. Res.* **36**, 73–78 (2016).
  - [11] J. Guo, G. Sun, B. Zhao, L. Wang, W. Hong, V. A. Sidorov, N. Ma, Q. Wu, S. Li, Z. Y. Meng, A. W. Sandvik, and L. Sun, “Quantum phases of  $\text{SrCu}_2(\text{BO}_3)_2$  from high-pressure thermodynamics,” *Phys. Rev. Lett.* **124**, 206602 (2020).
  - [12] S. Toth and B. Lake, “Linear spin wave theory for single- $Q$  incommensurate magnetic structures,” *J. Phys.: Condens. Matter* **27**, 166002 (2015).
  - [13] C. Boos, S. P. G. Crone, I. A. Niesen, P. Corboz, K. P. Schmidt, and F. Mila, “Competition between intermediate plaquette phases in  $\text{SrCu}_2(\text{BO}_3)_2$ ,” *Phys. Rev. B* **100**, 140413(R) (2019).
  - [14] P. Corboz and F. Mila, “Tensor network study of the Shastry-Sutherland model in zero magnetic field,” *Phys. Rev. B* **87**, 115144 (2013).
  - [15] K. Kodama, M. Takigawa, M. Horvatić, C. Berthier, H. Kageyama, Y. Ueda, S. Miyahara, F. Becca, and F. Mila, “Magnetic superstructure in the two-dimensional quantum antiferromagnet  $\text{SrCu}_2(\text{BO}_3)_2$ ,” *Science* **298**, 395 (2002).
  - [16] E. Manousakis, “The spin-1/2 Heisenberg antiferromagnet on a square lattice and its application to the cuprous oxides,” *Rev. Mod. Phys.* **94**, 1 (1991).
  - [17] J. D. Reger and A. P. Young, “Monte Carlo simulations of the spin- $\frac{1}{2}$  Heisenberg antiferromagnet on a square lattice,” *Phys. Rev. B* **37**, 5978 (1988).
  - [18] A. W. Sandvik, “Finite-size scaling of the ground-state parameters of the two-dimensional Heisenberg model,” *Phys. Rev. B* **56**, 11678 (1997).